

Topological surface states in epitaxial $(\text{SnBi}_2\text{Te}_4)_n (\text{Bi}_2\text{Te}_3)_m$ natural van der Waals superlattices

Sotirios Fragkos ^{1,2,*}, Laëtitiya Baringthon ^{3,4}, Polychronis Tsipas ¹, Evangelia Xenogiannopoulou ¹, Patrick Le Fèvre,⁴ Praveen Kumar,⁵ Hanako Okuno,⁵ Nicolas Reyren,³ Aristide Lemaitre,⁶ Gilles Patriarche,⁶ Jean-Marie George ³ and Athanasios Dimoulas¹

¹*Institute of Nanoscience and Nanotechnology, National Center for Scientific Research “Demokritos,” 15310 Athens, Greece*

²*Department of Mechanical Engineering, University of West Attica, 12241 Athens, Greece*

³*Unité Mixte de Physique, CNRS, Thales, Université Paris-Saclay, 91767 Palaiseau, France*

⁴*Synchrotron SOLEIL, L’Orme des Merisiers, 91192 Gif-sur-Yvette, France*

⁵*Interdisciplinary Institute of Research of Grenoble, Commissariat à l’Énergie Atomique et aux Énergies Alternatives, 38054 Grenoble, France*

⁶*Université Paris-Saclay, CNRS, Centre de Nanosciences et de Nanotechnologies, 91120 Palaiseau, France*



(Received 4 September 2020; accepted 24 December 2020; published 14 January 2021)

Topological insulators are good candidates for charge to spin conversion with high efficiency due to their spin-polarized topological surface states (TSSs). In this work, we provide experimental evidence for two-dimensional (2D) TSSs in $(\text{SnBi}_2\text{Te}_4)_n (\text{Bi}_2\text{Te}_3)_m$ natural van der Waals superlattices grown by molecular beam epitaxy using angle resolved photoelectron spectroscopy and magnetotransport. While the TSSs overlap with bulk conduction band (BCB) states at the Fermi energy, it is shown that by increasing the Sn composition, the influence of BCB states is reduced and becomes minimum for SnBi_2Te_4 . The latter compound, found to be in the form of septuplet layers, shows weak antilocalization effect with a prefactor $\alpha \sim -0.41$, indicating that the TSSs and the bulk behave as one 2D channel in which magnetotransport properties are influenced by large spin-orbit coupling.

DOI: [10.1103/PhysRevMaterials.5.014203](https://doi.org/10.1103/PhysRevMaterials.5.014203)

I. INTRODUCTION

Three-dimensional (3D) topological insulators (TIs) have topological surface states (TSSs) with their spin locked to the orbital momentum due to large spin-orbit coupling (SOC), offering high charge to spin conversion efficiency [1,2] via the Edelstein effect [3]. Therefore, among other applications, they could be ideal candidates to replace heavy metals (Pt, Ta, etc.) in spin-orbit torque (SOT) magnetic devices [2]. Archetypical 3D TIs such as the layered Bi_2Se_3 and Bi_2Te_3 show promise [2] but their use for practical applications is hampered by the parasitic contribution from the bulk conduction band (BCB). Mixing with other compounds is a means to tailor the surface topological properties in favor of the TSS contribution in the electronic transport. It has been shown, for example [4], that doping Bi_2Te_3 with 0.9% Sn brings the Fermi level inside the bulk energy gap, therefore crossing only the TSSs and thus avoiding BCB contribution. The TSSs and bulk electronic band structure in compounds containing more Sn at stoichiometric compositions such as the Bi-rich SnBi_2Te_4 , SnBi_4Te_7 , etc., or in alloys with Sn-rich compositions [5] have not been experimentally investigated in detail. Notably, the parent SnTe is also a topological crystalline insulator (TCI) [6], which creates the prospect that TSSs can be obtained over the entire range of Sn composition x (0–1). From previous works on similar compounds PbBi_2Te_4 , PbBi_4Te_7 , GeBi_4Te_7 , and MnBi_2Te_4 [7–11], it is expected that the Sn-Bi-Te mixed compound will take the form of a natural van der Waals

heterostructure of the general form $(\text{SnBi}_2\text{Te}_4)_n (\text{Bi}_2\text{Te}_3)_m$ where n layers of SnBi_2Te_4 alternate with m layers of Bi_2Te_3 . The first member of the series, SnBi_2Te_4 ($n = 1, m = 0$) forms a septuplet Te-Bi-Te-Sn-Te-Bi-Te where SnTe takes the middle position at the septuplet layer when it mixes with Bi_2Te_3 , while the second member of the series, SnBi_4Te_7 ($n = 1, m = 1$) forms a natural van der Waals superlattice where one SnBi_2Te_4 septuplet alternates with one Bi_2Te_3 quintuplet. Higher-order members of the series [e.g., $\text{SnBi}_6\text{Te}_{10}$ ($n = 1, m = 2$)] form natural van der Waals superlattices where one SnBi_4Te_7 septuplet alternates with two or more Bi_2Te_3 quintuplets [5]. Theoretical investigations of the different members of the series have been presented showing that they are all TIs with the Fermi level lying in the gap [5,12]. The first member of the series, SnBi_2Te_4 , has already been grown in bulk form (nanoplates) [13] and a weak antilocalization (WAL) effect has been observed in magnetotransport measurements, attributed to TSSs possibly intermixed with bulk contributions. In addition, it has been shown [13] that the bulk SnBi_2Te_4 deviates from ideal since a cation exchange occurs and the middle row of the septuplet is occupied by both Sn and Bi with Sn presence being dominant. No experimental data are available regarding the electronic band structure and the presence of TSSs in any member of the series. A direct observation of the TSSs by ARPES and their correlation with magnetotransport are required in order to confirm a substantial contribution of TSSs to electronic conduction, necessary for SOT devices and spintronics. Moreover, all work so far has been performed on bulk materials grown in equilibrium [13–16]. Epitaxial thin films grown by out-of-equilibrium techniques such as molecular beam epitaxy (MBE) could add

*s.fragkos@inn.demokritos.gr

TABLE I. Samples grown by MBE for various thicknesses determined by HRTEM and XRD, and their Bi/Sn ratios estimated by *in situ* XPS.

Sample	Thickness d (nm)	Bi/Sn ratio
S1	~20 (HRTEM)	–
S2	10.2 (XRD)	3.27
S3	~22 (HRTEM)	3.21
S4	16.2 (XRD)	2.03
S5	~22 (HRTEM)	1.98
S6	~10 (HRTEM)	0.57
S7	3.8 (XRD)	3.05
S8	5.9 (XRD)	1.80

flexibility in tailoring the natural van der Waals superlattice structure and their topological properties and open the route for scalable large area growth of composite TI/magnetic layer devices.

In the present work, we report on the structure and the electronic properties, especially those related to the TSSs, of four different TI compounds and alloys, namely, Bi_2Te_3 , SnBi_4Te_7 , SnBi_2Te_4 , and $\text{Sn}_{1-x}\text{Bi}_x\text{Te}$ grown by molecular beam epitaxy on $\text{InAs}(111)/\text{Si}(111)$ substrates. The layered structure is studied by high-resolution scanning transmission electron microscopy (STEM) revealing a layer stacking in the form of natural van der Waals superlattice. Combining first-principles calculations with *in situ* and synchrotron ARPES, we confirm the presence of TSSs and correlate them with magnetotransport measurements. By varying the Bi/Sn ratio and monitored by ARPES, we are able to tune the position of the Fermi level with respect to the TSSs and the BCB allowing the identification of Sn composition at which the TSS contribution maximizes relative to BCB.

II. RESULTS

A. Epitaxial growth and natural van der Waals superlattice

Eight samples were grown (see Sec. IV) on $\text{InAs}(111)$ substrates with different Bi/Sn ratios and four of them were studied in detail (Table I). Their Bi/Sn ratio is determined by x-ray photoelectron spectroscopy (XPS) using sensitivity factors from the literature confirming the nominal ratio estimated from the evaporation rates (Fig. S1 in the Supplemental Material (SM) [17]). Sn composition is controlled by the deposition rates of Sn relative to Bi. Te is supplied under conditions of overpressure such that the growth rate ratio $Te/M \sim 15$ ($M = \text{Bi}, \text{Sn}$). Under these conditions, Te is incorporated in the material to obtain the targeted stoichiometric compounds while the excess Te with low sticking coefficient is desorbed.

Technologically important epitaxial $\text{InAs}(111)$ on $\text{Si}(111)$ substrates are used in this work. The InAs substrates offer an excellent template for the epitaxial growth of chalcogenides. The chalcogen atoms (Se, Te) are often used for the passivation of GaAs and related compounds, including InAs prior to MBE growth because they saturate dangling bonds without reacting with the substrate. Therefore, chalcogenides such as ZrTe_2 and MoTe_2 [18,19] 2D materials form clean and sharp interfaces with excellent epitaxial order [18]. In addition,

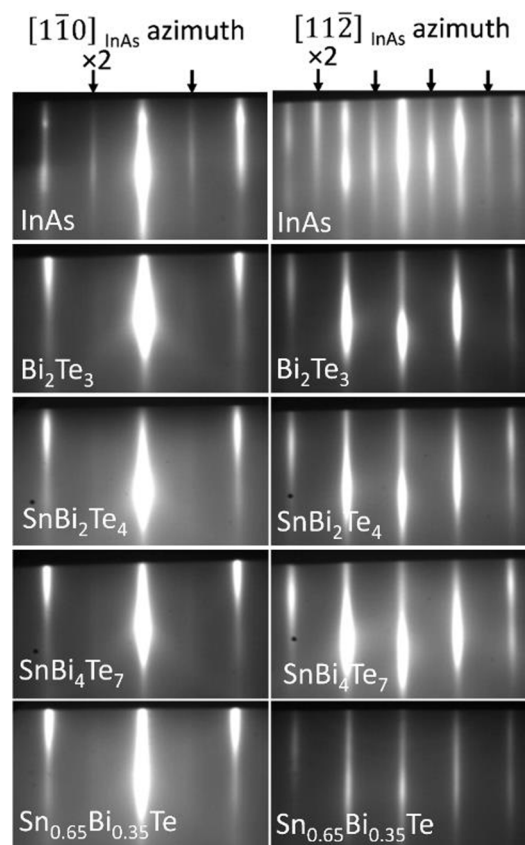


FIG. 1. RHEED patterns of $\text{InAs}(111)$ substrate and Sn-Bi-Te films along the InAs $[1 \bar{1} 0]$ and $[1 1 \bar{2}]$ azimuths.

there is a nearly lattice matching condition between the InAs and Bi_2Te_3 (Fig. 1) that makes this substrate suitable for the epitaxial growth of Bi_2Te_3 and Sn-containing compounds. In order to ensure that neither In or As is segregated from the substrate into the epitaxial films during the growth, In $3d$ and As $2p$ peaks were studied in detail using XPS for bare $\text{InAs}(111)$ and samples S3 and S8 (Fig. S2 in the SM [17]). The thickness of the InAs used in this work is 35 nm.

Substrates are treated (see Sec. IV) so that a clean $\text{InAs}(111)$ surface is obtained prior to growth, as indicated by the $\times 2$ reconstruction pattern of the reflection high-energy electron-diffraction (RHEED) in Fig. 1. RHEED also indicates a good in-plane alignment between the layers and the substrate along crystallographic dimensions of high symmetry. The good matching of the streak positions indicates that all compounds have very similar lattice constants. The latter have the tendency to increase as the Sn composition is increased. In addition, RHEED indicates a nearly lattice matching condition between the layers and the substrate. Using the in-plane lattice constant $a = 4.284 \text{ \AA}$ of InAs as reference, the respective of Bi_2Te_3 , SnBi_2Te_4 , SnBi_4Te_7 , and $\text{Sn}_{0.64}\text{Bi}_{0.36}\text{Te}$ are estimated to be 4.343, 4.392, 4.403, and 4.475 \AA .

The microstructure is investigated by cross-sectional high-resolution scanning transmission electron microscopy (STEM). The data for SnBi_2Te_4 and SnBi_4Te_7 are presented in Figs. 2 and 3, respectively. Images of Bi_2Te_3 and $\text{Sn}_{0.64}\text{Bi}_{0.36}\text{Te}$ are shown in Figs. S3 and Fig. S4 of the SM [17]. SnBi_2Te_4 [Fig. 2(a)] shows a layered structure with

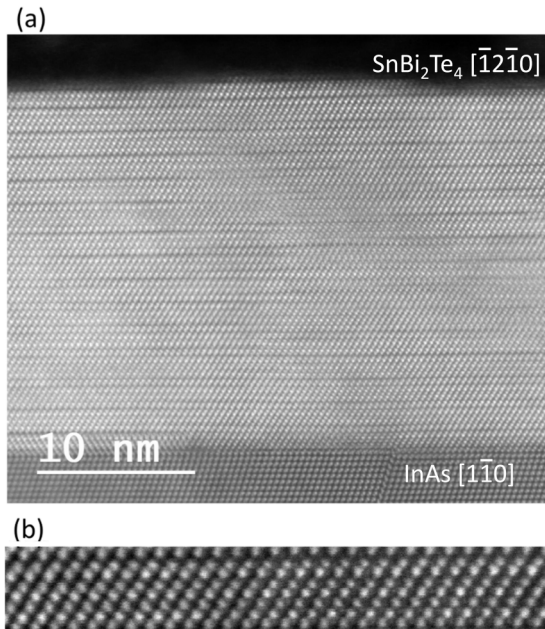


FIG. 2. (a) High-resolution cross-section STEM image of layered SnBi_2Te_4 (sample S5). (b) Detail of one septuplet layer showing a seven-row arrangement of the form Te-MII-Te-MI-Te-MII-Te. The metal positions MI and MII are preferentially occupied by Sn and Bi, respectively.

small van der Waals gap (sample S5). Each layer [Fig. 2(b)] is a septuplet (SL) consisting of seven atom rows, four occupied by Te atoms and the rest by the metal atoms Bi and Sn. The septuplet structure is in distinct difference with the quintuplet (QL) structure of the parent Bi_2Te_3 (Fig. S3 in the SM [17]). The septuplet structure is also confirmed by x-ray diffraction (Fig. S5 in the SM [17]) where a pure phase of the seven-

layer structure is confirmed over the entire film area without contributions from other phases (e.g., quintuplet Bi_2Te_3 -like phase). The septuplet arrangement indicates a tendency to form an ordered alloy where Sn ideally occupies the middle row. It should be noted that the substrate surface roughness influences the film microstructure as can be seen in Fig. S3 [17]. Therefore, the quintuplets are slightly distorted appearing as being nonparallel to each other.

However, deviation from this ideal configuration occurs as discussed below in Fig. 3 where the Bi-rich SnBi_4Te_7 is depicted. To accommodate the surplus of Bi, SnBi_4Te_7 adopts a natural van der Waals superlattice structure where septuplets of SnBi_2Te_4 alternate with quintuplets of Bi_2Te_3 [Figs. 3(a) and 3(b)] (sample S3). The order has a very frequent occurrence although it is not sustained throughout the entire film thickness. For example, near the top right part of the film imaged in Fig. 3, the top three layers have an SL/SL/SL stacking followed by QL/SL/SL configuration; then the film shows the tendency to form almost ideally alternating SL/QL structure in the bottom part near the interface. An analysis of the intensity of the high-angle annular dark field image [Fig. 3(c)] reveals that the SnBi_2Te_4 septuplet layer deviates from the model structure according to which Sn occupies preferably the middle row, while Bi occupies the rows labeled MII [Fig. 3(d)]. In the model configuration, the intensity of the middle row would be expected to be low, even lower than the intensity of the Te rows. On the contrary, the intensity of the middle row is high, suggesting that there is a significant exchange between Bi and Sn so the metal positions MI and MII are occupied by both Sn and Bi atoms [Fig. 3(b)]. It should be noted that an exchange between Bi and Sn occurs also in the bulk-grown SnBi_2Te_4 nanoplates [13].

When Sn content increases beyond the SnBi_2Te_4 composition (sample S6, Table I), the Sn-rich alloy adopts a three-dimensional cubic crystal structure (Fig. S4 in the SM [17]) rather than a layered one, very similar to the parent SnTe compound [20–22].

B. First-principles calculations

Ab initio calculations are focused on SnBi_4Te_7 and SnBi_2Te_4 , since the parent Bi_2Te_3 and SnTe TIs are well studied materials [20–23]. The topological nature of SnBi_4Te_7 and SnBi_2Te_4 is determined by calculating the \mathbb{Z}_2 topological invariants (see Sec. IV) in the $k_z = 0$ and $k_z = \pi$ planes. For the $k_z = 0$ plane, $\mathbb{Z}_2 = 1$, while for the $k_z = \pi$ plane, $\mathbb{Z}_2 = 0$. Therefore, a band order inversion occurs, resulting in a non-trivial band gap and the appearance of surface states. The band inversion between $\bar{\Gamma}_9$ and $\bar{\Gamma}_8$ is further confirmed by using related software available from the Bilbao Crystallographic server [24,25] in order to calculate the irreducible representations, where the materials are classified as strong TIs, meaning that the TSSs, for both materials, are time-reversal symmetry protected. No band inversion is predicted in M and L time-reversal invariant momentum points.

The electronic band structure of SnBi_4Te_7 (trigonal space group $P\bar{3}m1$) calculated by DFT along the $K\Gamma L$ and HAL directions [Fig. 4(a)] of the Brillouin zone (BZ) [Fig. 4(b)] shows a global band gap of ~ 0.1 eV. The projected BZ calculation [Fig. 4(c)] reveals two different TSSs depending on

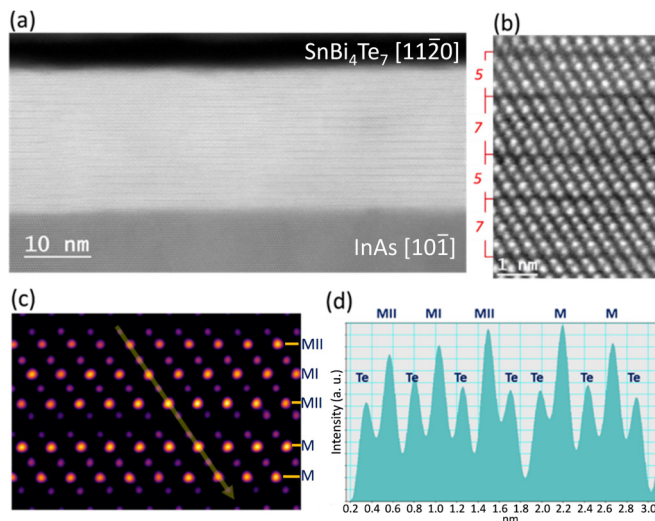


FIG. 3. (a) High-resolution cross-section image of SnBi_4Te_7 (sample S3). (b) HR STEM shows alternating QL and SL layers in the form of a natural van der Waals (vdW) superlattice where each layer is separated by a vdW gap. (c) High-angle annular dark field (HAADF) image and (d) the intensity line profile along a yellow arrow in (c) showing a possible atom exchange between Sn and Bi in the middle row of the SL.

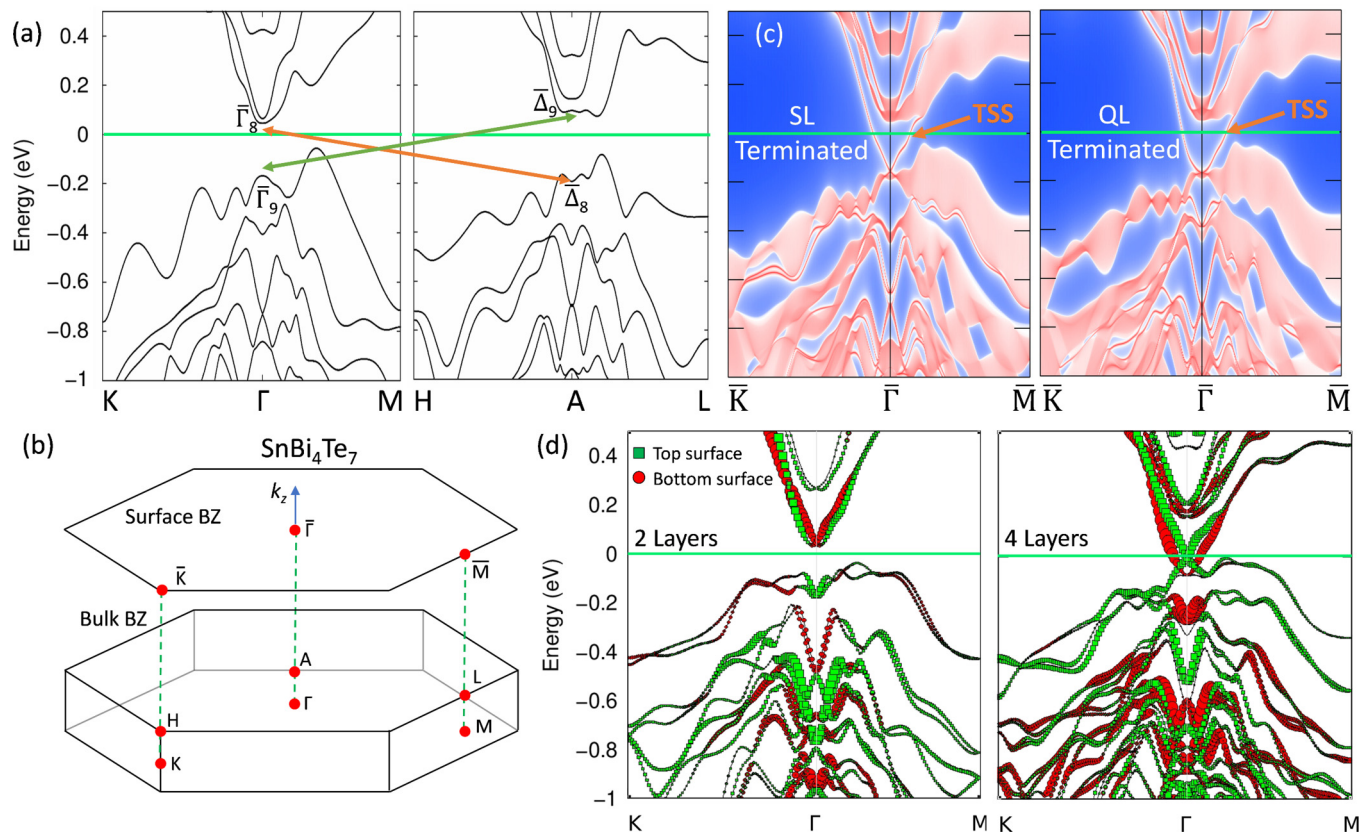


FIG. 4. (a) The calculated band structure of bulk SnBi_4Te_7 along the $K\Gamma L$ and HAL directions showing the band inversion (green and orange lines). (b) The first BZ, (c) the projected Brillouin zone along the $\bar{K}\bar{\Gamma}\bar{M}$ direction of the two different terminations, and (d) the band structures of the non-inversion-symmetric two and four layers. The green and red symbols correspond to the atomic orbitals of the top and bottom surfaces, respectively. It should be noted that no overlap between the CB and VB is predicted and the calculated Fermi level does not cross either the conduction or the valence band.

whether the surface is SL or QL terminated. While the bulk material is centrosymmetric, thin films with an even number of layers (e.g., SL/QL, SL/QL/SL/QL, etc.) lack inversion symmetry and their bands near the Fermi level are split reflecting the two different TSSs at the top and bottom surface [Fig. 4(d)]. This is potentially interesting since it results in (near) energy degeneracies at the Fermi level which could have a large contribution to the spin Hall conductivity of this material. However, it should be noted that for any real system, the film-substrate interaction already splits the Dirac cones of the top and bottom surfaces due to inversion-symmetry breaking.

Like its parent compound Bi_2Te_3 , SnBi_2Te_4 crystallizes in a rhombohedral structure with space group $R\bar{3}m$. The calculated band structures of bulk SnBi_2Te_4 along the $K\Gamma L$ and KZX directions of the BZ [Fig. 5(a)] are illustrated in Fig. 5(b) and a band gap of 0.1–0.2 eV is observed. By calculating the projection of the BZ along the $\bar{K}\bar{\Gamma}\bar{M}$ direction [Fig. 5(c)] a small overlap between valence and conduction bands appears, which vanishes in smaller thicknesses as indicated in Fig. 5(d).

C. Topological surface states imaging by ARPES

The electronic band structure is systematically investigated as a function of Sn composition at room temperature using

in situ ARPES with He I excitation at 21.22 eV and at 15 K using synchrotron ARPES with variable photon energy.

It is generally observed [Figs. 6 and 7] that two different states coexist at the Fermi surface near the center of the BZ. One of these states with a triangular shape reflects the trigonal symmetry of the bulk material; therefore it is attributed to the BCB. The BCB is clearly distinguished from the other state with a hexagonal symmetry which is attributed to a surface band. The surface nature of the latter band is further confirmed by ARPES since it remains invariant to the photon excitation energy. This can be seen in Fig. 6(c) where the k_z - k_y (parallel to the ΓZ and ΓK planes) Fermi surface map at E_F [Fig. 6(c)] is obtained by scanning the photon energy from 19 to 80 eV with horizontal polarization for an inner potential $V_0 = 8.5$ eV (see details in Sec. IV), while recording the photoelectron intensity for all momenta k_y along $\bar{\Gamma}\bar{K}$. The map shows two nearly parallel lines independent of the photon energy, confirming that the hexagonal feature is a surface state. The horizontal intensities located around $k_z \sim 2.5 \text{ \AA}^{-1}$ are attributed to resonances of Bi $5d$ and Sn $4d$ core levels and around $k_z \sim 3.0 \text{ \AA}^{-1}$ to resonances of Te $4d$ core levels. Also, no bulk band dispersion is observed in the $k_z - k_y$ Fermi surface map, because as observed in the contour plot [Fig. 6(b)], the contribution of bulk states is more pronounced in the corners of the hexagonal feature along the $\bar{\Gamma}\bar{M}$ direction, while the contribution at the center of the BZ and along the

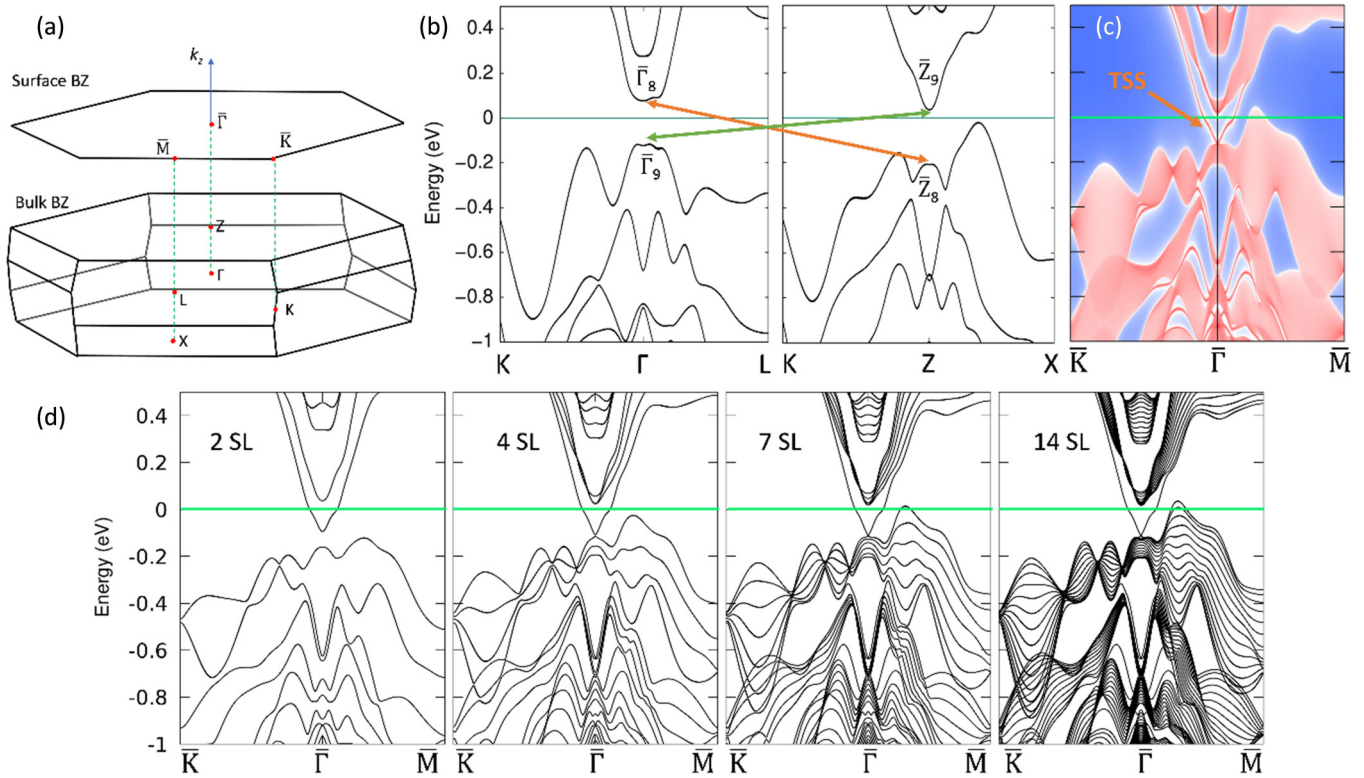


FIG. 5. (a) The BZ of SnBi₂Te₄. (b) The calculated band structure of bulk SnBi₂Te₄ along the $K\Gamma L$ and KZX directions and showing the band inversion (green and orange lines). (c) The projection of the Brillouin zone along the $\bar{K}\bar{\Gamma}\bar{M}$ direction and (d) the band structure of two, four, seven, and 14 SLs.

ΓK direction is negligible. The dispersion of the bulk states is seen more clearly at the Fermi surface plots at different photon energies (Fig. S6 in the SM [17]) where the bulk conduction bands change shape and intensity depending on the photon energy.

A direct comparison with the DFT calculations [Figs. 4(c) and 5(c)], reveals that the hexagonally shaped surface band inside the bulk band gap is in fact a topological surface state.

In the case of SnBi₄Te₇, the Fermi level does not cross the valence band in agreement with the DFT predictions. However, in the case of SnBi₂Te₄, the DFT prediction that the valence band maxima [Fig. 5(c)] disperse above the Fermi level is not confirmed by ARPES for all sample thickness investigated from 11 SLs down to two SLs. The discrepancy between theory and experiment is attributed to the well-known band gap underestimation in the local density approximation

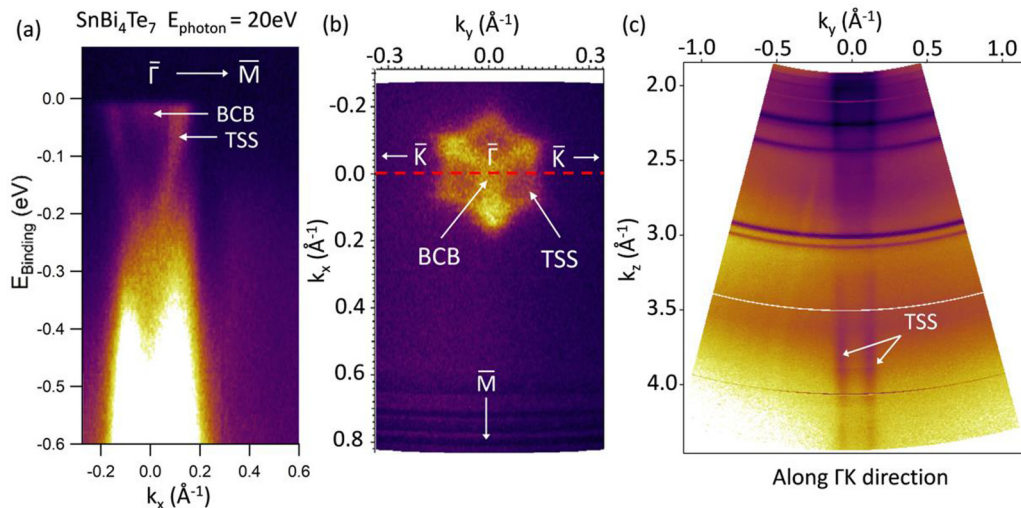


FIG. 6. (a) ARPES spectra of SnBi₄Te₇ for photon energy $E_{\text{photon}} = 20 \text{ eV}$ along $\bar{\Gamma}\bar{M}$ and (b) the Fermi surface of the same sample. (c) The photon energy dependent $k_z - k_y$ Fermi surface map at E_F (k_y parallel to $\bar{\Gamma}\bar{K}$). The traces of the topological surface states (TSS) are recorded at the k_y values at which the dashed red line in (b) cuts the trace of the surface state. BCB denotes the bulk conduction band states.

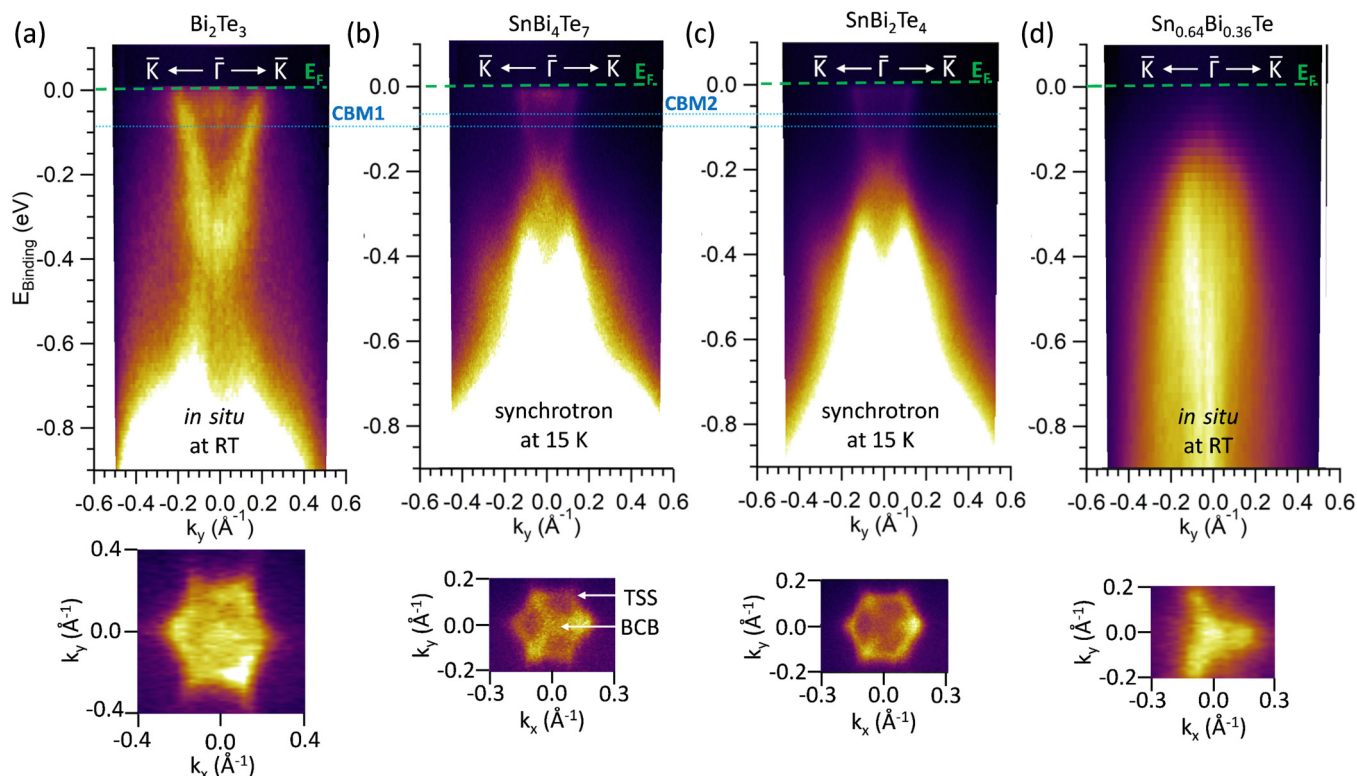


FIG. 7. (a)–(d) ARPES measurements of band dispersions and their k_x - k_y Fermi surface maps for four samples with different Sn compositions recorded along $\bar{K}\bar{\Gamma}\bar{K}$. The shifts of the conduction band minimum are indicated with horizontal blue dotted lines. TSS and BCB in (b) denote the topological surface states and bulk conduction band, respectively.

(LDA) and generalized-gradient approximation with Perdew-Burke-Ernzerhof (GGA PBE) functionals [26]. It should be noted that it is not possible to distinguish the termination of the top surface of SnBi_4Te_7 with ARPES, since the surface of the material is not perfectly flat. Some areas on the sample are terminated with Bi_2Te_3 and some other neighboring areas are terminated with SnBi_2Te_4 . Even in the ideal case of a flat surface, it would have been very difficult to directly compare with DFT since the difference between the two terminations predicted by DFT [Fig. 4(d)] is very small and the ARPES resolution is inadequate to distinguish between the two terminations.

The shape and intensity of TSS and BCB energy dispersions do not depend on the thickness (Fig. S7 in the SM [17]), but rather appear to be in correlation with the Sn composition in Bi-rich compounds. More specifically, the BCB is less pronounced, essentially less intense, in SnBi_2Te_4 compared to SnBi_4Te_7 and Bi_2Te_3 (Fig. 7). The conduction band minimum (CBM) shifts to higher energy as Sn composition increases, barely crossing the Fermi level for the SnBi_2Te_4 compound with the highest Sn composition. The same behavior is observed in the Fermi surface plots of Fig. 7 where the intensity of the trigonal-shaped BCB decreases as Sn composition increases and becomes barely visible in the SnBi_2Te_4 compound where the TSSs becomes the dominant contribution at the Fermi surface. Using Luttinger's theorem [27–29], the 2D electron density of the TSSs is estimated from ARPES measurements at the Fermi surface as $n_{2D} = A_F/(4\pi^2)$, where A_F is the area in the momentum space of the closed orbit at the

Fermi level approximated by the hexagon (Figs. 6 and 7). The electron densities are found to be $n_{2D} = 1.37(\pm 0.2) \times 10^{13} \text{ cm}^{-2}$ for SnBi_2Te_4 and $n_{2D} = 1.40(\pm 0.25) \times 10^{13} \text{ cm}^{-2}$ for SnBi_4Te_7 . To obtain these values we considered a nondegenerate (spin-polarized) TSS band at the top surface which is the only band contributing to ARPES.

By further increasing Sn in the $\text{Sn}_{0.64}\text{Bi}_{0.36}\text{Te}$ alloy, the TSS with the hexagonal symmetry disappears and the ARPES spectral weight is dominated by the trigonally shaped valence band states as expected, since the sample adopts a cubic 3D SnTe-like structure where a valence band maximum appears at $\bar{\Gamma}$ [23]. In short, SnBi_2Te_4 presents a pronounced TSS with the least interference from BCB states at the Fermi energy. Therefore, SnBi_2Te_4 compound shows the strongest influence from TSSs and it is worth investigating its magnetotransport properties with the aim to correlate the observed TSSs with transport properties (see next section). This claim is further supported by imaging the energy and momentum distribution curves at the Fermi level and around the Γ point, respectively, for samples S1, S2, S4, and S6 (Fig. S8 in the SM [17]).

The evolution of crystal and band structure with composition (Bi/Sn ratio) is demonstrated in Fig. 8. This summarizes our study, showing that by varying the Bi/Sn ratio, we are able to move from one end compound to another, by growing in between a natural van der Waals superlattice where one SnBi_2Te_4 septuplet alternates with one Bi_2Te_3 quintuplet, and also tuning the position of the Fermi level with respect to the TSSs and the BCB.

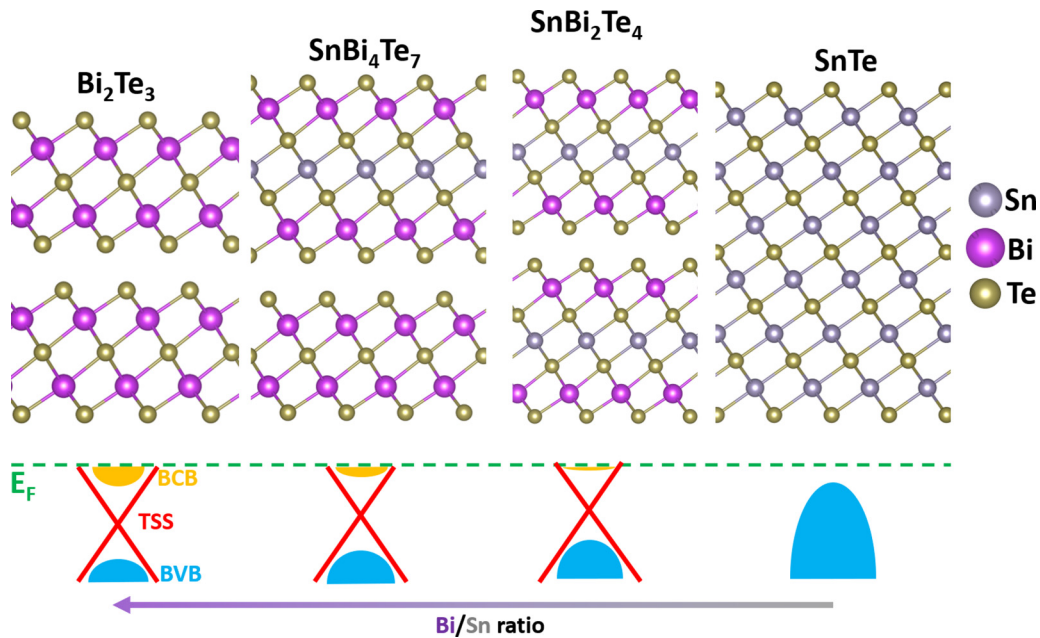


FIG. 8. Schematic illustration showing the evolution of crystal and band structure as a function of Bi/Sn ratio.

D. Topological surface states' contribution in magnetotransport

After the ARPES study, the sample was protected with 3 nm Al deposited by MBE *in situ*. The Al was then naturally oxidized in air. The sample was then patterned in a Hall bar for the magnetoresistance study. Magnetoresistance measurements at low temperature (6 K) for SnBi_2Te_4 are presented in Fig. 9. The raw data in Fig. S9 of the SM [17] indicate that the main contribution in Hall resistance comes from the antisymmetric part which is further analyzed here. The antisymmetric part of Hall resistance in Fig. 9(a) is nonlinear, indicating that at least two types of carriers contribute. The fitting reveals that the two types of carriers are both electrons, one with a large density attributed to the BCB $n_{\text{BCB}} = -4.69(\pm 0.1) \times 10^{14} \text{ cm}^{-2}$ and low mobility $\mu_{\text{BCB}} = 43.2(\pm 2) \text{ cm}^2 \text{ V}^{-1} \text{ s}^{-1}$, and the other with a lower density $n_{\text{TSS}} = -6.9(\pm 0.03) \times 10^{12} \text{ cm}^{-2}$ and higher mobility $\mu_{\text{TSS}} = 1260(\pm 2) \text{ cm}^2 \text{ V}^{-1} \text{ s}^{-1}$. The latter density n_{TSS} agrees within a factor of 2 with the TSS density $n_{2D} = 1.37 \times 10^{13} \text{ cm}^{-2}$

estimated from ARPES (see previous section). Because the surface changed from ARPES to transport measurement (Al capping), this discrepancy can be ascribed to band bending [30]. In order to calculate the carrier density from Hall resistance, we assumed TSSs with in-plane helical spin-orbit coupling, ignoring possible out-of-plane spin components. Therefore, the contribution to the Hall resistance of the low electron density is attributed to the 2D TSS. The higher electron density is considered to be a contribution from BCB, which is also present in the ARPES measurements at the Fermi level. The appearance of only two distinct carrier contributions in the Hall data attributed to TSS and BCB imply that a possible unoxidized Al cap may not have an effect on magnetotransport; otherwise an additional (third) type of carrier would have been observed, which is not the case here.

Figure 9(b) shows the magnetoresistance of SnBi_2Te_4 for out-of-plane ($B \perp I$, blue curve) and in-plane ($B \parallel I$, red curve) magnetic field B . A magnetoresistance dip in the low

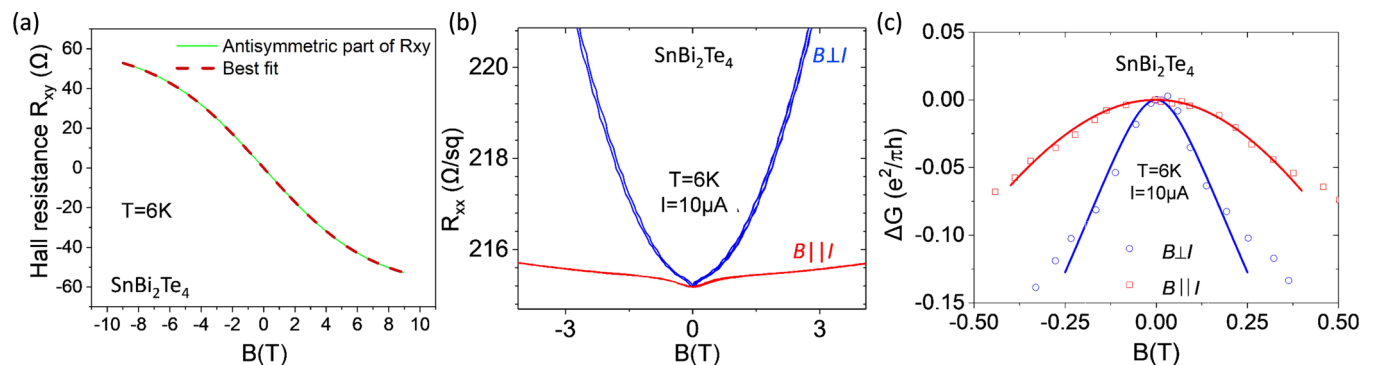


FIG. 9. Magnetotransport measurements of SnBi_2Te_4 at 6 K. (a) Hall resistance (R_{xy}) displaying characteristic bent shape (nonlinear) due to multiband conduction. (b) Longitudinal resistance (R_{xx}) as a function of the in-plane and out-of-plane field revealing the WAL effect. (c) Magnetoconductance ΔG normalized by $e^2/(\pi h)$ as a function of the magnetic field, where blue and red lines correspond to fitting curves.

magnetic fields ($|B| < 0.25$ T) appears in both orientations: It is attributed to the weak antilocalization (WAL) effect [31] as a result of the large SOC in topological insulators [Fig. 9(b)]. While the appearance of a dip in $B \perp I$ is associated with a 2D TSS, the emergence of a similar magnetoresistance dip in parallel magnetic fields is an indication that a WAL effect originating from the bulk SnBi_2Te_4 contributes to the conductance in addition to TSSs [31–33].

Figure 9(c) shows the magnetoconductance ΔG as a function of the magnetic field, which, in a rough approximation, is derived from the measured magnetoresistance using [34]

$$\Delta G = \frac{1}{R(\theta, B)} - \frac{1}{R(\theta, 0)}. \quad (1)$$

The experimental curves are fitted using Eqs. (2) and (3) for out-of-plane and in-plane B field, respectively,

$$\Delta G_{\perp}(B) \approx \alpha_{\perp} \frac{-e^2}{\pi h} \left[\psi \left(\frac{1}{2} + \frac{B_{\Phi}}{B} \right) - \ln \left(\frac{B_{\Phi}}{B} \right) \right], \quad (2)$$

$$\Delta G_{\parallel}(B) \approx \alpha_{\parallel} \frac{-e^2}{\pi h} \ln \left(1 + \beta \frac{ed^2}{4\hbar B_{\Phi}} B^2 \right), \quad (3)$$

where $B_{\Phi} = \hbar/(4el_{\Phi}^2)$, l_{Φ} is the phase coherence length, and ψ is the digamma function. We find α_{\perp} and l_{Φ} by fitting the magnetoconductance to the Hikami-Larkin-Nagaoka (HLN) formula [Eq. (2)] [35,36] for the perpendicular magnetic field and then α_{\parallel} and β ($0 < \beta < 1$) by fitting the magnetoconductance for the parallel magnetic field to Eq. (3) [36–38] with $l_{\Phi} \sim 52$ nm being determined from Eq. (2). This is only an approximation, since in general, l_{Φ} for in-plane longitudinal transport is expected to be different compared to the one for transverse transport across the film thickness due to film anisotropy. From Eqs. (2) and (3) the values of prefactors α_{\perp} and α_{\parallel} , -0.42 and -0.39 , are obtained, respectively. Our results agree well with the data reported for bulk-grown SnBi_2Te_4 nanoplates [13].

More specifically, in Ref. [12] the MR dip is also present in both orientations of the B field and the fitting yields $\alpha = -0.4$, and $l_{\Phi} = 108.4$ nm. In the present work, the perpendicular and in-plane field measurements yield similar values of α which are very close to -0.5 , indicating that the system behaves as a single transport channel system [39] where the two surfaces are connected through the bulk. A value of $\beta = 0.24$ is determined from Eq. (3), a parameter which is related to the surface state penetration depth revealing thus the correlation strength between the upper and the lower TSSs. The higher this correlation, the closer the parameter β approaches the value 1 [39].

Zeeman and electron-electron interaction effects were ignored in the analysis of perpendicular magnetoresistance data since they are suppressed in perpendicular magnetic fields [34]. On the other hand, these effects are considered to introduce parabolic dependence of parallel magnetoconductance for low magnetic field strength [34,40,41], which, however, is not observed in our films. This led to the conclusion that the influence of these effects is rather small. Moreover, electron-electron interactions are expected [41] in films < 6 nm, considerably thinner than the ones used in this work (~ 22 nm).

III. METHODS

A. Film growth and surface preparation

The InAs(111)/Si(111) substrates were chemically cleaned in a 5 N HF solution in isopropyl alcohol for 5 min to etch the surface oxide and subsequently rinsed in isopropyl alcohol for 30 s in order to avoid reoxidation of the substrate. An annealing step at 400 °C in UHV follows to get a clean and flat InAs(111) (In-terminated) surface as evidenced by RHEED. Where appropriate, mild Ar+ sputtering was used ($E \approx 1.5$ keV, $p \approx 2 \times 10^{-5}$ mbar, $t \approx 30$ s) prior to the annealing step to obtain a clean surface as evidenced by a 2×2 reconstruction in RHEED pattern attributed to In surface vacancies [42]. The films are grown under Te-rich conditions in an UHV MBE (DCA Instruments) vertical chamber. The base pressure of the system is $\sim 5 \times 10^{-10}$ mbar. Bi and Te (99.999%) are evaporated from a Knudsen cell and Sn from an e -beam evaporator.

B. STEM characterization

STEM measurements have been performed using Cs-corrected Themis (Thermo Fisher) at 200 keV. HAADF-STEM images were acquired using a convergence semiangle of 20 mrad and collecting scattering > 55 mrad. STEM specimens were prepared by the focused ion beam (FIB) lift-out technique using a Cross-Beam 750 (ZEISS) at 30 kV followed by a cleaning at 5 kV.

Other samples were also observed in an aberration-corrected FEI TITAN 200 Themis microscope operating at 200 keV in the STEM mode with a probe current of 70 pA and a probe size of 0.09 nm at the full width at half maximum. The convergence half angle of the probe was 17.6 mrad and the detection inner and outer half angles for HAADF STEM were 69 and 200 mrad, respectively. All micrographs were 2048×2048 pixels. The dwell time was 8 μ s and the total acquisition time was 41 s. Lamellae for STEM observation were prepared from the sample using focused ion beam (FIB) ion milling and thinning. Prior to FIB ion milling, the sample surface was coated with a carbon film to protect the surface from the platinum mask deposited used for the ion milling process. Ion milling and thinning were carried out in a FEI SCIOS dual-beam FIB SEM. Initial etching was performed at 30 keV, and final polishing was performed at 5 keV. The lamellae were prepared following the $\langle 110 \rangle$ zone axis of the silicon substrate.

C. X-ray diffraction (XRD)

X-ray diffraction was performed with a laboratory diffractometer (Bruker D8) with a $\text{Cu } K\alpha$ source.

D. Magnetotransport

Samples are lithographed in Hall bars, 50 width by 150 length μm^2 , allowing precise control of the current uniformity and direction. We used a dc current source and nanovoltmeters to measure simultaneously the transverse and longitudinal resistance. The magnetic field is provided by a superconducting coil and the sample is mounted on a goniometer in order to vary the field direction relative to the

current one. To insure proper electrical contacts, contacts were prepared using lift-off of Ti(20 nm)/Au(150 nm) Au deposited using evaporation.

E. ARPES measurements

Specially prepared samples with 20-nm-thick Te capping were measured at the SOLEIL-Synchrotron facility “CASSIOPEE,” after capping removal, with horizontally polarized light and variable photon energy from 19 to 80 eV in order to follow the electronic band dispersion along the k_z axis. The measurements were carried out at $T = 15$ K and the energy resolution was 15 meV with a polar angle step of 0.2° . The value of the inner potential V_0 is usually determined based on some periodicity in the k_z scan. Here, since we are dealing with a surface state, there is no obvious periodicity in the scan. Therefore, we employed a different methodology [43] to estimate V_0 from $V_0 = |E_0| + \Phi$ where E_0 corresponds to the energy of the bottom of the valence band referenced to the Fermi level and Φ , the material work function. By combining our ARPES and our DFT calculations we estimate $E_0 = 3.5$ eV at $k_{\parallel} = 0 \text{ \AA}^{-1}$ and from ultraviolet photoelectron spectroscopy (UPS) we estimate $\Phi = 5$ eV, so $V_0 = 8.5$ eV. Then, k_z as a function of photon energy $h\nu$ for perpendicular emission (i.e., $k_{\parallel} = 0 \text{ \AA}^{-1}$) is obtained as in Ref. [43] from $k_z = \sqrt{\frac{2m}{\hbar^2}(E_k + V_0)}$, where m is the effective mass of electrons inside the solid and E_k is the kinetic energy of the emitted electrons, which satisfies $E_k = h\nu - \Phi - E_B$, where E_B is the electron binding energy. Results of synchrotron radiation ARPES data are presented in Figs. 6 and 7 of the main text.

The *in situ* ARPES measurements were carried out at room temperature with a 100 mm hemispherical electron analyzer equipped with a 2D charge-coupled device (CCD) detector (SPECS) without breaking the vacuum. The He I (21.22 eV) resonant line is used to excite photoelectrons. The energy resolution of the system is better than 40 meV with a polar angle step of 1° .

F. First-principles calculations

The first-principles calculations were performed using the Vienna *Ab Initio* Simulation Package [44,45] and projector-augmented waves [46]. The generalized-gradient approximation with Perdew-Burke-Ernzerhof [47] parametrization was used as the exchange correlation functional. The kinetic energy cutoff was set at 500 eV, using the Monkhorst-Pack scheme [48] employing a $9 \times 9 \times 9k$ -point mesh. The atomic positions were fully optimized by conjugate gradient, using a force threshold of $10^{-3} \text{ eV \AA}^{-1}$. The maximally localized Wannier functions are fitted based on the s and p orbitals of Sn, Bi, and Te atoms using the WANNI90 code [49] and the \mathbb{Z}_2 and the projected Brillouin zone calculations were carried out by the WANNIERTOOLS software [50]. Spin-orbit coupling was included in band structure calculations.

IV. DISCUSSION AND CONCLUSIONS

In this work, it is confirmed by TEM and XRD that MBE-grown SnBi_2Te_4 thin films form septuplet layers separated

from each other by a van der Waals gap. Further analysis of the TEM images reveals that Sn occupies predominately the middle row although significant exchange with Bi occurs similar to those also observed in bulk-grown SnBi_2Te_4 nanoplates [13]. On the other hand, the Bi-rich SnBi_4Te_7 compound is ordered in the form of natural van der Waals superlattices where SnBi_2Te_4 septuplets alternate with Bi_2Te_3 quintuplets. The ARPES measurements reveal the existence of TSSs in SnBi_2Te_4 and SnBi_4Te_7 which slightly overlap with BCB states at the Fermi level. The electronic band structure near the Fermi level shows little or no correlation with the thickness. On the other hand, films with higher Sn content corresponding to the SnBi_2Te_4 compound present the minimum overlap with the BCB states at the Fermi energy so they could be considered as more suitable for applications which are based on the TSS electronic transport properties.

Further evidence of the TSSs in the SnBi_2Te_4 compound has been obtained from magnetotransport measurements. A nonlinear Hall resistance [Fig. 9(a)] indicates the presence of two types of carriers (electronlike). One of them with the highest mobility of $1260 \text{ cm}^2 \text{ V}^{-1} \text{ s}^{-1}$ has a concentration of $6.9 \times 10^{12} \text{ cm}^{-2}$ which is only a factor of ~ 2 smaller than the value of $1.37 \times 10^{13} \text{ cm}^{-2}$ estimated from ARPES for the 2D TSS, attributed to the different band bending [30] caused by the Al capping which is added after ARPES for the transport measurements. Based on the aforementioned, it is concluded that the 2D TSS probed by ARPES correlates well with the high-mobility carriers revealed from Hall measurements.

Additional information is obtained from longitudinal magnetoresistance. A resistance dip near zero magnetic field $B (< 0.25 \text{ T})$ appearing in both $B \perp I$ and $B \parallel I$ configurations is attributed to a weak antilocalization (WAL) effect originating from the strong spin-orbit coupling in this material. In general, the appearance of a dip in the $B \parallel I$ measurement is considered to be an indication [29,31,32] of a bulk contribution in addition to the contribution from the TSSs.

Conclusions about the different contributions can be extracted from the values of the measured α and β prefactors. A value of $\alpha \sim -0.5$ indicates contribution from one 2D channel only, while $\alpha = -1$ signifies the additive contribution of two independent 2D channels [29,40]. Although typically in the literature analysis is mainly based on the parameter α , the value of β gives important information too. The latter parameter measures the extent of TSS penetration inside the film [39]. Then, a large value of $\beta \sim 1$ indicates that there is a strong coupling between the top and bottom TSSs leading to a single 2D TSS channel transport. In our films though, the measured $\beta = 0.24$ is rather small indicating that the two TSSs contribute independently to magnetotransport, in which case, we would expect $\alpha \sim -1$. However, the measured value of α is ~ -0.42 , close to -0.5 which is typically valid for one 2D channel contribution. It is therefore concluded that the whole film with $d < l_\phi$ consisting of two interfaces and one bulk contribution behaves as one 2D channel with $\alpha = -0.42$ as also argued previously for Bi_2Se_3 [39].

The behavior in our SnBi_2Te_4 films is similar to that obtained in thick ($\sim 50 \text{ nm}$) Bi_2Te_3 films [31,32]. Notably, for thinner Bi_2Te_3 films ($\sim 5 \text{ nm}$) a sole contribution from 2D TSS, acting as one channel, has been reported [31,51],

suggesting that thinning SnBi₂Te₄ down to a few nanometers could be a viable route to isolate a pure 2D TSS transport.

It should be mentioned that in several materials, a transition from a WAL to a weak localization (WL) regime occurs leading to negative magnetoresistance at higher magnetic fields, due to enhanced disorder and lack of topological protection [52,53]. With rare exceptions [31,32,51], in TIs, including our SnBi₂Te₄ in the present work, such transition is absent, and the behavior is characterized by a zero-field dip followed by a parabolic behavior to higher fields. This is considered as evidence that there is sufficient topological protection of TSSs in our films that prevents the crossover from WAL to WL regimes.

ACKNOWLEDGMENTS

We acknowledge the Horizon 2020 FETPROAC Project No. SKYTOP-824123 “Skyrmion—Topological Insulator and Weyl Semimetal Technology,” the FLAG-ERA project MELoDICA, the Hellenic Foundation for Research and Innovation, and the General Secretariat for Research and

Technology, under Grant No. 435 (2D-TOP). This work was also supported by computational time granted from the Greek Research and Technology Network in the National High-Performance Computing facility ARIS under Project No. 2D-TOP. The support by a public grant overseen by the French National Research Agency (ANR) as part of the “Investissements d’Avenir” program (Labex NanoSaclay, Reference No. ANR-10-LABX-0035).

S.F. contributed to DFT calculations, synchrotron and *in situ* ARPES measurements, and data analysis. L.B. contributed to ARPES and magnetotransport measurements. P.T. contributed to sample growth, *in situ* ARPES and XPS measurements, and data analysis. E.X. contributed to sample growth, synchrotron ARPES, and *in situ* XPS measurements. P.L.F. contributed to synchrotron ARPES measurements. P.K. and H.O. contributed to STEM characterization. N.R. contributed to magnetotransport measurements and XRD measurements. A.L. and G.P. contributed to STEM characterization. J.-M.G. contributed to magnetotransport measurements and A.D. contributed to sample growth, DFT calculations, *in situ* ARPES measurements, and data analysis.

-
- [1] N. H. D. Khang, Y. Ueda, and P. N. Hai, *Nat. Mater.* **17**, 808 (2018).
- [2] Y. Wang, R. Ramaswamy, and H. Yang, *J. Phys. D: Appl. Phys.* **51**, 273002 (2018).
- [3] J.-C. Rojas-Sánchez, S. Oyarzún, Y. Fu, A. Marty, C. Vergnaud, S. Gambarelli, L. Vila, M. Jamet, Y. Ohtsubo, A. Taleb-Ibrahimi, P. Le Fèvre, F. Bertran, N. Reyren, J.-M. George, and A. Fert, *Phys. Rev. Lett.* **116**, 096602 (2016).
- [4] Y. L. Chen *et al.*, *Science* **325**, 178 (2009).
- [5] M. G. Vergniory, T. V. Menshchikova, I. V. Silkin, Yu. M. Koroteev, S. V. Eremeev, and E. V. Chulkov, *Phys. Rev. B* **92**, 045134 (2015).
- [6] Y. Tanaka, Z. Ren, T. Sato, K. Nakayama, S. Souma, T. Takahashi, K. Segawa, and Y. Ando, *Nat. Phys.* **8**, 800 (2012).
- [7] K. Kuroda, H. Miyahara, M. Ye, S. V. Eremeev, Yu. M. Koroteev, E. E. Krasovskii, E. V. Chulkov, S. Hiramoto, C. Moriyoshi, Y. Kuroiwa, K. Miyamoto, T. Okuda, M. Arita, K. Shimada, H. Namatame, M. Taniguchi, Y. Ueda, and A. Kimura, *Phys. Rev. Lett.* **108**, 206803 (2012).
- [8] S. V. Eremeev, Y. M. Koroteev, and E. V. Chulkov, *JETP Lett.* **92**, 161 (2010).
- [9] D. Souchay *et al.*, *J. Mater. Chem. C* **7**, 9939 (2019).
- [10] Y. Deng, Y. Yu, M. Z. Shi, Z. Guo, Z. Xu, J. Wang, X. H. Chen, and Y. Zhang, *Science* **367**, 895 (2020).
- [11] S.-Y. Xu *et al.*, [arXiv:1007.5111](https://arxiv.org/abs/1007.5111).
- [12] M. G. Vergniory, T. V. Menshchikova, S. V. Eremeev, and E. V. Chulkov, *Appl. Surf. Sci.* **267**, 146 (2013).
- [13] Y.-C. Zou *et al.*, *Nano Res.* **11**, 696 (2018).
- [14] L. Pan, J. Li, D. Berardan, and N. Dragoe, *J. Solid State Chem.* **225**, 168 (2015).
- [15] R. Vilaplana *et al.*, *J. Alloys Compd.* **685**, 962 (2016).
- [16] V. L. Kuznetsov, L. A. Kuznetsova, and D. M. Rowe, *J. Phys. D: Appl. Phys.* **34**, 700 (2001).
- [17] See Supplemental Material at <http://link.aps.org/supplemental/10.1103/PhysRevMaterials.5.014203> for supporting experimental details.
- [18] P. Tsipas, D. Tsoutsou, S. Fragkos, R. Sant, C. Alvarez, H. Okuno, G. Renaud, R. Alcotte, T. Baron, and A. Dimoulas, *ACS Nano* **12**, 1696 (2018).
- [19] P. Tsipas, S. Fragkos, D. Tsoutsou, C. Alvarez, R. Sant, G. Renaud, H. Okuno, and A. Dimoulas, *Adv. Funct. Mater.* **28**, 1802084 (2018).
- [20] S.-Y. Xu *et al.*, *Nat. Commun.* **3**, 1192 (2012).
- [21] S. Fragkos, R. Sant, C. Alvarez, E. Golias, J. Marquez-Velasco, P. Tsipas, D. Tsoutsou, S. Aminalragia-Giamini, E. Xenogiannopoulou, H. Okuno, G. Renaud, O. Rader, and A. Dimoulas, *Phys. Rev. Mater.* **3**, 104201 (2019).
- [22] J. Wang, N. Wang, H. Huang, and W. Duan, *Chin. Phys. B* **25**, 117313 (2016).
- [23] M. Z. Hasan and C. L. Kane, *Rev. Mod. Phys.* **82**, 3045 (2010).
- [24] M. G. Vergniory, L. Elcoro, C. Felser, N. Regnault, B. A. Bernevig, and Z. Wang, *Nature* **566**, 480 (2019).
- [25] M. G. Vergniory, L. Elcoro, Z. Wang, J. Cano, C. Felser, M. I. Aroyo, B. A. Bernevig, and B. Bradlyn, *Phys. Rev. E* **96**, 023310 (2017).
- [26] J. P. Perdew, *Int. J. Quantum Chem.* **28**, 497 (1985).
- [27] M. Ben Shalom, A. Ron, A. Palevski, and Y. Dagan, *Phys. Rev. Lett.* **105**, 206401 (2010).
- [28] M. Kang, B. Kim, S. H. Ryu, S. W. Jung, J. Kim, L. Moreschini, C. Jozwiak, E. Rotenberg, A. Bostwick, and K. S. Kim, *Nano Lett.* **17**, 1610 (2017).
- [29] E. Lahoud, E. Maniv, M. Shaviv Petrushevsky, M. Naamneh, A. Ribak, S. Wiedmann, L. Petaccia, Z. Salman, K. B. Chashka, Y. Dagan, and A. Kanigel, *Phys. Rev. B* **88**, 195107 (2013).
- [30] Q. Barbedienne, J. Varignon, N. Reyren, A. Marty, C. Vergnaud, M. Jamet, C. Gomez-Carbonell, A. Lemaître, P. Le Fèvre, F. Bertran, A. Taleb-Ibrahimi, H. Jaffrès, J.-Marie George, and A. Fert, *Phys. Rev. B* **98**, 195445 (2018).
- [31] H.-T. He, G. Wang, T. Zhang, I.-K. Sou, G. K. L. Wong, J.-N. Wang, H.-Z. Lu, S.-Q. Shen, and F.-C. Zhang, *Phys. Rev. Lett.* **106**, 166805 (2011).
- [32] S.-P. Chiu and J.-J. Lin, *Phys. Rev. B* **87**, 035122 (2013).

- [33] H. Li, H.-W. Wang, Y. Li, H. Zhang, S. Zhang, X.-C. Pan, B. Jia, F. Song, and J. Wang, *Nano Lett.* **19**, 2450 (2019).
- [34] H. Tang *et al.*, *npj Quantum Mater.* **4**, 1 (2019).
- [35] S. Hikami, A. I. Larkin, and Y. Nagaoka, *Prog. Theor. Phys.* **63**, 707 (1980).
- [36] C. J. Lin, X. Y. He, J. Liao, X. X. Wang, V. Sacksteder IV, W. M. Yang, T. Guan, Q. M. Zhang, L. Gu, G. Y. Zhang, C. G. Zeng, X. Dai, K. H. Wu, and Y. Q. Li, *Phys. Rev. B* **88**, 041307(R) (2013).
- [37] B. L. Al'tshuler and A. G. Aronov, *JETP Lett.* **33**, 499 (1981).
- [38] V. K. Dugaev and D. E. Khmel'nitskiĭ, *Zh. Éksp. Teor. Fiz.* **86**, 1784 (1984).
- [39] A. Banerjee, O. Deb, K. Majhi, R. Ganesan, D. Senb, and P. S. A. Kumar, *Nanoscale* **9**, 6755 (2017).
- [40] M. Liu, C.-Z. Chang, Z. Zhang, Y. Zhang, W. Ruan, K. He, L.-l. Wang, X. Chen, J.-F. Jia, S.-C. Zhang, Q.-K. Xue, X. Ma, and Y. Wang, *Phys. Rev. B* **83**, 165440 (2011).
- [41] J. Wang, A. M. DaSilva, C.-Z. Chang, K. He, J. K. Jain, N. Samarth, X.-C. Ma, Q.-K. Xue, and M. H. W. Chan, *Phys. Rev. B* **83**, 245438 (2011).
- [42] A. Tagushi and K. Kanisawa, *Appl. Surf. Sci.* **252**, 5263 (2006).
- [43] A. Damascelli, *Phys. Scr.* **109**, 61 (2004).
- [44] G. Kresse and J. Furthmüller, *Comput. Mater. Sci.* **6**, 15 (1996).
- [45] G. Kresse and J. Furthmüller, *Phys. Rev. B* **54**, 11169 (1996).
- [46] P. E. Blöchl, *Phys. Rev. B* **50**, 17953 (1994).
- [47] J. P. Perdew, K. Burke, and M. Ernzerhof, *Phys. Rev. Lett.* **77**, 3865 (1996).
- [48] H. Monkhorst and J. Pack, *Phys. Rev. B* **13**, 5188 (1976).
- [49] A. A. Mostofi, J. R. Yates, Y.-S. Lee, I. Souza, D. Vanderbilt, and N. Marzari, *Comput. Phys. Commun.* **185**, 2309 (2014).
- [50] Q. S. Wu, S. N. Zhang, H.-F. Song, M. Troyer, and A. A. Soluyanov, *Comput. Phys. Commun.* **224**, 405 (2018).
- [51] A. Roy, S. Guchhait, S. Sonde, R. Dey, T. Pramanik, A. Rai, H. C. P. Movva, L. Colombo, and S. K. Banerjee, *Appl. Phys. Lett.* **102**, 163118 (2013).
- [52] K. Banerjee, J. Son, P. Deorani, P. Ren, L. Wang, and H. Yang, *Phys. Rev. B* **90**, 235427 (2014).
- [53] H. B. Zhang, J. D. Yao, J. M. Shao, and G. W. Yang, *J. Phys. D: Appl. Phys.* **49**, 095003 (2016).